Available online at www.sciencedirect.com
SCIENCE DIRECT®
PERGAMON
International Journal of Heat and Mass Transfer 46 (2003) 1183–1197
International Journal of HEAT and MASS TRANSFER
www.elsevier.com/locate/ijhmt

A direct three-dimensional simulation of radiation-induced natural convection in a shallow wedge

Chengwang Lei *, John C. Patterson

School of Engineering, James Cook University, Townsville, Qld. 4811, Australia

Received 27 August 2001; received in revised form 30 August 2002

Abstract

A three-dimensional numerical simulation is carried out to investigate the natural convection in a shallow wedge subject to solar radiation. The study reveals three distinct stages of the flow development from an isothermal and stationary state: an initial stage, a transitional stage and a quasi-steady stage. The heat transfer at the initial stage is dominated by conduction from the sloping bottom. The transitional stage starts with the onset of instabilities, and the quasi-steady state is characterised by steady growth of a spatially averaged temperature. The present results have confirmed the earlier observations in a flow visualisation experiment and a two-dimensional simulation.

1. Introduction

This study considers the unsteady natural convection in a wedge subject to solar radiation. It is motivated by interest in understanding the buoyancy-induced heat and mass transport in littoral waters [1–5]. The daytime heating model developed by Farrow and Patterson [5], who presented an asymptotic solution based on the assumption of small bottom slopes, is reinvestigated here with a direct numerical procedure. In this model, the incident surface radiation was absorbed by the water body according to Beer's law (see Section 2 for details). This model took explicit account of the depth dependent absorption of the radiation, which closely represented reality. In addition, it assumed that any residual radiation at the bottom was absorbed by the bottom and the absorbed energy was re-emitted as a heat flux. This flux was greater at the shallow end than at the deeper, and gave rise to a destabilizing temperature gradient at the bottom.

It is clear that this daytime heating model is driven by both internal buoyancy sources and a boundary heat flux. In this case, there are competing stability effects: the stabilizing effect of the stratification introduced by the absorption of solar radiation in the upper part of the water column and the destabilizing effect of the bottom boundary heat flux. The understanding of the fluid dynamics for this problem has great significance due to its special geometry and complex forcing conditions. Although this problem is framed in the context of the near shore transport question, it is clearly relevant to any buoyancy driven flow in which these competing stability effects are present, and therefore the present study should find broader applications.

It is worth noting here that the absorption of incident radiation imposes a natural length scale appropriate to the radiation and the fluid, i.e. the attenuation length. Typically in natural water bodies, this length scale is $O(1–2\ \mathrm{m})$, i.e. most of the radiation is absorbed between the surface and this depth. Consequently, a water body with a sloping bottom may be separated into two regions: the first, a shallow region near the shore in which the forcing is dominated by the boundary flux mechanism described above; and a second deeper region in which the incident radiation serves only to stratify the upper part of the water body, with the motions being passively driven by the events of the first region. In the early study reported in [5], a semi-infinite wedge which covered both the shallow and deeper regions was

* Corresponding author. Tel.: +61-7-4781-4172; fax: +61-7-4775-1184.
E-mail address: chengwang.lei@jcu.edu.au (C. Lei).

0017-9310/03/$ - see front matter
PII: S0017-9310(02)00401-5

Nomenclature

A	bottom slope, $A = h^*/L^* = h/L$
C_p	specific heat (J/kg°C)
g	acceleration due to gravity (m/s^2)
Gr	Grashof number, $Gr = g\beta H_0 h^4/(\nu^2 k)$
H	dimensionless heat transfer rate
H_0	volumetric heating intensity at the surface (m°C/s), $H_0 = I_0/(\rho_0 C_p)$
I, I_0	radiation intensity at a given water depth and water surface (W/m^2)
k	thermal diffusivity (m^2/s)
L, W, h	dimensionless length, width and maximum water depth of the wedge
L^*, W^*, h^*	length, width and maximum water depth of the wedge (m)
n^*	coordinate normal to the bottom (m)
p	dimensionless pressure
p^*	pressure (N/m^2)
Pr	Prandtl number, $Pr = \nu/k$
Q	dimensionless flow rate
t	dimensionless time
t^*	time (s)
T	dimensionless temperature
T^*	temperature (°C)
T_0	starting water temperature (°C)
$\overline{T}$	spatially averaged temperature (°C)
u, v, w	dimensionless velocity components in x, y and z directions
u^*, v^*, w^*	velocity components in x^*, y^* and z^* directions (m/s)
x, y, z	dimensionless coordinates
x^*, y^*, z^*	coordinates in horizontal, vertical and transverse directions (m)

Greek symbols

β	coefficient of thermal expansion (1/°C)
ϕ	any quantity of the flow
η	dimensionless bulk attenuation coefficient for water
η^*	bulk attenuation coefficient for water (1/m)
ν	kinematic viscosity (m^2/s)
ρ_0	density (kg/m^3)
τ	dimensionless temperature variation
τ^*	temperature variation (°C)

Superscript

*	dimensional quantities

Subscripts

x, y, z	partial derivatives with respect to a spatial direction
t	partial derivatives with respect to time

considered, whereas in this study only the shallow region affected by the bottom heat flux is concerned. The fluid dynamics and major scales in shallow waters subject to solar radiation has been discussed in detail by Lei and Patterson [6].

Lei and Patterson [7] also conducted a model experiment to visualise the convection process in a shallow triangular cavity driven by the aforementioned combination of forcing mechanisms. The experiment was conducted in an $L^* \times W^* \times h^* = 0.6$ m $\times$ 0.3 m $\times$ 0.06 m perspex tank with a fixed bottom slope of $A = 0.1$ (see Nomenclature and Fig. 1 for definitions and dimensions). The tank was filled with water originally in an isothermal and stationary state. The solar radiation was simulated using a spot theatre lamp. A constant radiation with an intensity of $I_0 = 50$ W/m^2 was applied instantaneously on the water surface. The bottom of the tank was made black so that it absorbed any residual radiation reaching the bottom. The convective flow was then visualised using a shadowgraph technique, and temperatures were measured simultaneously at discrete locations along the sloping bottom. Three distinct stages, an initial stage, a transitional stage and a quasi-steady stage, of the flow development were identified from the experiment. The initial stage is characterised by domination by conduction near the bottom boundary, resulting in the growth of a thermal layer there. The transitional stage is characterised by the presence of instabilities emanating from the bottom boundary which are manifested as rising plumes translating up the slope. The quasi-steady state is characterised by a steady rise in average temperature and quasi-regular presence of instabilities with reduced intensities.

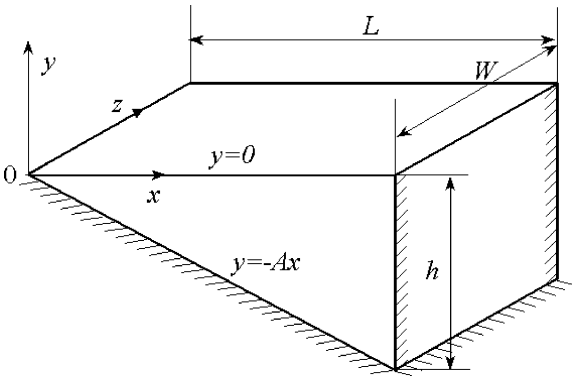

Fig. 1. Geometry of the physical domain.

The above experiment was reproduced in a two-dimensional (2-D) simulation [8], and the numerical results clearly indicated a three-stage development of the convective flow, confirming the experimental observations based on the shadowgraph visualisation. However, the application of a 2-D model for an essentially three-dimensional (3-D) experiment has limited the accountability of the numerical simulation. Moreover, the features of the 3-D convective instability as observed in the experiment cannot be fully resolved in the 2-D simulation.

The present investigation is a corresponding 3-D numerical simulation of the previously reported experiment [7]. In this study, the full 3-D governing equations are solved directly with high order numerical schemes. The detail of the numerical procedures is given in Section 2, and the numerical results are presented in Section 3, which also compares the 3-D simulation with the previous experiment and 2-D simulation. The application of a direct numerical procedure allows a detailed examination of the flow features without imposing restrictions to the system parameters and simplifying the forcing model.

2. Formulation and numerical procedures

A 3-D wedge (see Fig. 1) with rigid non-slip boundaries at the bottom and end and an open boundary at the top is considered. The wedge is filled with water initially at rest and at temperature T_0. At time $t^* = 0$, a surface radiation of intensity I_0 is initiated and thereafter maintained. When the radiation travels through a water column, the radiation intensity at a particular wavelength decreases with depth according to Beer's law [5,9,10]:

$$I = I_0 e^{\eta^* y^*} \quad (y^* \leqslant 0) \tag{1}$$

The attenuation coefficient for water is strongly dependent on the wavelength of the radiation and the turbidity of water [10]. However, it is assumed here that the absorption of the solar radiation is characterised by a single bulk attenuation coefficient, which is a common practice in most limnological applications and also consistent with the previous 2-D simulation [8]. The shallow wedge assumption implies that the water depth is less than the attenuation length of the radiation, i.e. $h^* < 1/\eta^*$. In this case, a significant amount of radiation reaches the sloping bottom.

The subsequent flow and temperature changes within the wedge are governed by the 3-D Navier–Stokes equations and energy equation with Boussinesq assumptions:

$$\frac{\partial u^*}{\partial t^*} + u^*\frac{\partial u^*}{\partial x^*} + v^*\frac{\partial u^*}{\partial y^*} + w^*\frac{\partial u^*}{\partial z^*} = -\frac{1}{\rho_0}\frac{\partial p^*}{\partial x^*} + \nu\nabla^2 u^* \tag{2}$$

$$\frac{\partial v^*}{\partial t^*} + u^*\frac{\partial v^*}{\partial x^*} + v^*\frac{\partial v^*}{\partial y^*} + w^*\frac{\partial v^*}{\partial z^*} = -\frac{1}{\rho_0}\frac{\partial p^*}{\partial y^*} + \nu\nabla^2 v^* + g\beta(T^* - T_0) \tag{3}$$

$$\frac{\partial w^*}{\partial t^*} + u^*\frac{\partial w^*}{\partial x^*} + v^*\frac{\partial w^*}{\partial y^*} + w^*\frac{\partial w^*}{\partial z^*} = -\frac{1}{\rho_0}\frac{\partial p^*}{\partial z^*} + \nu\nabla^2 w^* \tag{4}$$

$$\frac{\partial T^*}{\partial t^*} + u^*\frac{\partial T^*}{\partial x^*} + v^*\frac{\partial T^*}{\partial y^*} + w^*\frac{\partial T^*}{\partial z^*} = k\nabla^2 T^* + H_0\eta^* e^{\eta^* y^*} \tag{5}$$

$$\frac{\partial u^*}{\partial x^*} + \frac{\partial v^*}{\partial y^*} + \frac{\partial w^*}{\partial z^*} = 0 \tag{6}$$

The second term on the right-hand side of the energy Eq. (5) quantifies the absorption of radiation by the water [5].

The temperature and velocity boundary conditions for the present model are as follows (see also [5] except Item (4) for the boundary conditions on the transverse sidewalls):

(1) On the sloping bottom ($y^* = -Ax^*$), it is assumed that any residual radiation is fully absorbed by the bottom, which then immediately releases the energy back to the water in a form of a boundary heat flux. Accordingly, the boundary condition for the temperature is:

$$\frac{\partial T^*}{\partial n^*} = -\frac{H_0}{k} e^{-A\eta^* x^*} \quad (y^* = -Ax^*) \tag{7}$$

This boundary condition matches the black bottom model used in the experiment [7] and is approximately representative of reality. In field situations, the residual radiation reaching the bottom is either absorbed or reflected or scattered by the bottom. Most of the reflected and scattered radiation is ultimately absorbed by the water body, mainly by the lower layer near the bottom. The velocity conditions on the sloping bottom are those for a rigid non-slip wall, i.e. $u^* = v^* = w^* = 0$.

(2) The end-wall ($x^* = L^*$) is insulated, i.e. $\partial T^*/\partial x^* = 0$, and rigid non-slip velocity conditions apply to this boundary.

(3) On the water surface ($y^* = 0$), the heat loss through the surface is neglected. In other words, it is assumed that the water surface is insulated (i.e. $\partial T^*/\partial y^* = 0$). It is also assumed that the water surface is stress free ($\partial u^*/\partial y^* = \partial w^*/\partial y^* = 0$ and $v^* = 0$). The stress free surface condition is compatible with the previous experiment and also the field conditions in geophysical applications.

(4) In the transverse direction, periodic boundary conditions apply, i.e. $\phi(z^* = 0) \equiv \phi(z^* = W^*)$, where ϕ represents any quantity of the flow (u^*, v^*, w^*, T^*, p^* and their derivatives). The implementation of these conditions in our numerical simulations ensures up to the second derivatives are equal at the two ends in the transverse direction.

Since the water body in the wedge is heated continuously by absorbing the radiation penetrating through the water column and there is no heat loss through the boundaries, the water temperature will keep increasing without a limit, and there will be no steady state in terms of temperature. However, with a constant surface radiation being applied, a quasi-steady state may be reached in which the temperature increases at the same rate everywhere in the wedge whereas the temperature gradients and flow velocities become steady. The temperature variation can be split into two components:

$$T^* - T_0 = \overline{T}(t^*) + \tau^*(x^*, y^*, z^*, t^*) \tag{8}$$

i.e. a spatially averaged temperature which increases in time, and a spatial variation of temperature which has a steady state spatial distribution after a transition. The spatially averaged temperature $\overline{T}(t^*)$ can be obtained from a balance of energy entering from the surface and that absorbed by the water body, which gives $\overline{T}(t^*) = (2H_0/h^*)t^*$. It is seen that the average temperature in the tank increases linearly with time.

Substituting Eq. (8) into Eq. (5) yields an energy equation with respect to τ^*

$$\frac{\partial \tau^*}{\partial t^*} + u^*\frac{\partial \tau^*}{\partial x^*} + v^*\frac{\partial \tau^*}{\partial y^*} + w^*\frac{\partial \tau^*}{\partial z^*} = k\nabla^2\tau^* + (H_0\eta^* \mathrm{e}^{\eta^* y^*} - 2H_0/h^*) \tag{9}$$

Since all boundary conditions for the temperature (T^*) involve temperature gradients only and are independent of time, the same boundary conditions apply for τ^* as for T^* Eq. (9) is identical to Eq. (5) except that there is an extra term of heat sink on the right hand side. This is interpreted as placing a uniformly distributed heat sink equal to $2H_0/h^*$ across the enclosure while it is heated by the absorption of radiation entering from the surface. When the heat loss from the sink is balanced by the heat capture from the absorption of radiation, a steady state is reached for τ^*, corresponding to the quasi-steady state for T^*. In the following context, no distinction is made between the quasi-steady state for the temperature T^* and the steady state for the temperature τ^*. The complete system equations now consist of Eqs. (2), (3), (4), (9) and (6) with the term $(T^* - T_0)$ in Eq. (3) replaced by τ^*.

The quantities in the quasi-steady system equations are then normalised by the following scales: the length scale h^* the time scale $(h^*)^2/k$, the temperature variation scale H_0h^*/k, the velocity scale k/h^* the pressure gradient scale $\rho_0 g\beta H_0 h^*/k$ and the attenuation coefficient scale $(h^*)^{-1}$. The system equations are rewritten in dimensionless forms as follows:

$$u_t + uu_x + vu_y + wu_z = -(Pr^2Gr)p_x + Pr\nabla^2 u \tag{10}$$

$$v_t + uv_x + vv_y + wv_z = -(Pr^2Gr)p_y + Pr\nabla^2 v + (Pr^2Gr)\tau \tag{11}$$

$$w_t + uw_x + vw_y + ww_z = -(Pr^2Gr)p_z + Pr\nabla^2 w \tag{12}$$

$$\tau_t + u\tau_x + v\tau_y + w\tau_z = \nabla^2\tau + (\eta \mathrm{e}^{\eta y} - 2) \tag{13}$$

$$u_x + v_y + w_z = 0 \tag{14}$$

All quantities in Eqs. (10)–(14) are now dimensionless. The boundary conditions defined previously are also normalised with the same scales. The normalised governing equations are then solved together with normalised boundary conditions using a finite difference scheme. The velocity components and temperature are directly obtained from the Navier–Stokes equations and the energy equation, and the pressure is calculated from a pressure Poisson equation formed directly from the Navier–Stokes equations. The standard second-order central differencing scheme is used for all spatial derivatives except the non-linear terms in the momentum and energy equations, which are approximated with a modified second-order upwind scheme. The time integration for the velocity components and temperature is by a second-order time accurate backward differencing scheme. The system equations are solved implicitly with an iterative procedure. A successive over-relaxation method is used for all equations including the pressure Poisson equation. Details of the numerical schemes can be found in [11].

3. Numerical results

The experiment described in [7] is now simulated with the aforementioned numerical procedures. The calculation is conducted in a flow domain of dimensions corresponding to those of the experimental tank, i.e. $L = 10$, $W = 5$, $h = 1$ and $A = 0.1$. To avoid a singularity at the tip in numerical calculations, the tip is cut off at $x = 1$, and an extra rigid non-slip and adiabatic wall boundary is assumed here. It is anticipated that the flow in the interior of the domain is not modified significantly. The tank is filled with pure water, for which the dimensionless bulk attenuation coefficient is 0.37 (taken from the experimental configuration). The convective flow is calculated at $Gr = 2.51 \times 10^6$ and $Pr = 6.83$, which are also obtained from the experiment.

A non-uniform mesh is constructed for the modified physical domain so that nodes are effectively clustered to

the vicinities of all boundaries in the (x, y) plane. In the transverse direction, nodes are uniformly distributed. A test of mesh and time-step dependence is conducted prior to the calculation, and the results will be presented later in Section 3.5. Unless specified, the following results are obtained from an $81 \times 61 \times 41$ mesh with up to 15 nodes allocated within the bottom thermal boundary layer (based on the experimental measurement of [7]).

3.1. Early-stage flow

Similar to the 2-D simulation [8], the growth of a thermal boundary layer along the sloping bottom and the inception of a large-scale circulation across the enclosure can be identified at this stage.

3.1.1. Growth of the thermal boundary layer

The temperature structures within the wedge at the early stage after the initiation of the surface radiation are given in Fig. 2. Fig. 2a presents the iso-surfaces of temperatures $(\tau = 0)$ at $t = 0.001$ and 0.003 (corresponding to $t^* = 25$ and 76 s), while Fig. 2b presents shadowgraph images at the same stage (refer to [7] for details). Note that the times chosen from the numerical simulation (Fig. 2a) are different from those chosen from the experiment (Fig. 2b) although they are basically of the same order. We noticed that the flow development in the laboratory experiment is slightly ahead of that in the numerical simulation. Throughout this paper, the selection of numerical and experimental results for comparisons is based on the criterion that both results demonstrate the most important flow features at different stages of the flow development. The time indicated in the context should not be matched between the simulation and experiment. It is also noteworthy that the temperature data presented here is obtained by solving the quasi-steady state temperature equation (Eq. (13)), in which a heat sink is introduced to balance the linear growth of the spatially averaged temperature with time. A negative value of temperature $(\tau < 0)$ in the enclosure indicates a lower growth rate of the temperature relative to the mean growth across the tank, and a positive value $(\tau > 0)$ indicates a higher growth rate relative to the mean growth. Therefore, it is the relative value rather than the absolute value of the temperature that is meaningful to subsequent discussions.

In the present case, over 70% of the incident radiation reaches the bottom (estimated using Eq. (1)). The residual radiation is absorbed by the sloping bottom and then released back to the lower part of the water body. Therefore, a thermal boundary layer is expected to develop along the sloping bottom. This is clearly demonstrated in Fig. 2. It is observed from the numerical simulation that the temperature in a region close to the sloping bottom increases sharply at the early stage due to the diffusion of heat flux from the boundary. Apart

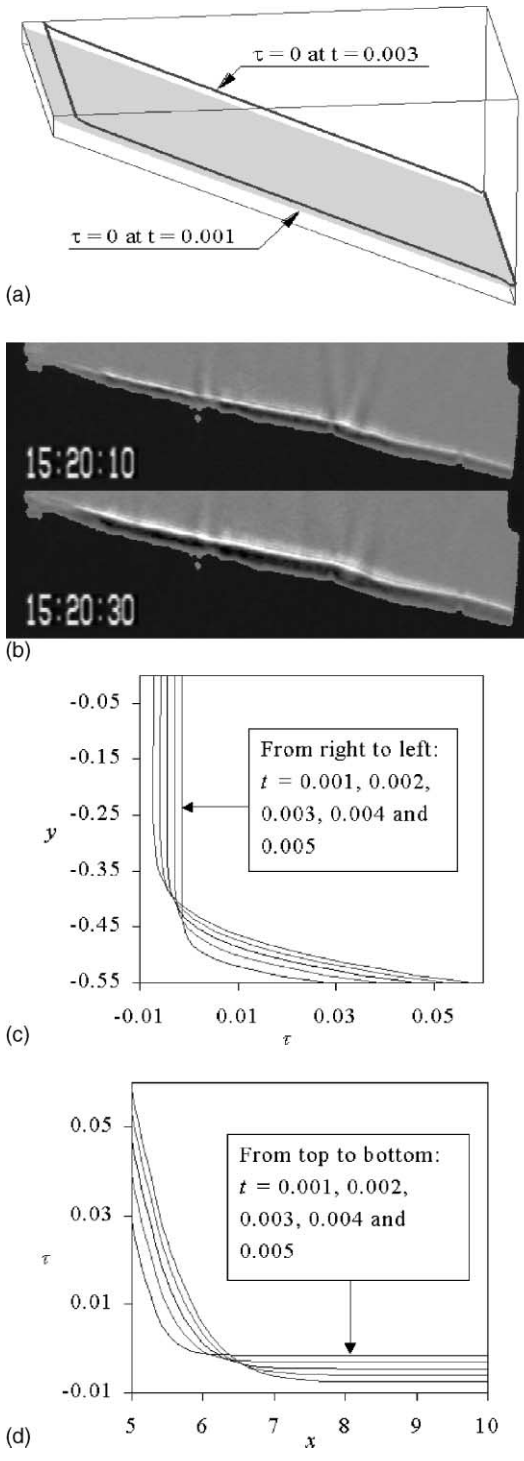

Fig. 2. Temperature structure at the early stage. (a) Iso-surfaces of temperatures at $t = 0.001$ and 0.003 ($t^* = 25$ and 76 s). (b) Shadowgraphs at 10 s (upper portion) and 30 s (lower portion) showing the growth of a thermal boundary layer. (c) Temperature profile along the vertical line $(x, z) = (5.5, 2.5)$. (d) Temperature profile along the horizontal line $(y, z) = (-0.5, 2.5)$.

from this boundary region which has positive temperatures, the temperatures in the rest of the enclosure are negative. Therefore, the core region and the thermal boundary layer are approximately separated by the $\tau = 0$ iso-surface. It is seen in Fig. 2a that the iso-surface of $\tau = 0$ quickly moves away from the sloping bottom, indicating a rapid expansion of the thermal boundary layer, which is in good agreement with the shadowgraph visualisation (refer to Fig. 2b and also [7]). On the shadowgraphs (Fig. 2b), the thermal boundary layer and the core region were separated by a narrow bright band, which was also seen to quickly move away from the boundary during the experiment. Therefore, the width of the dark band immediately underneath the bright band approximately indicated the thickness of the thermal boundary layer. It is also found in the numerical simulation that the temperature variation in the negative region is negligible compared with that of the boundary region, suggesting that the bottom heating is dominating the radiation absorption by the water column at the early stage.

Two more conclusions can be drawn from the temperature structure presented in Fig. 2a: first, the temperature structure is purely 2-D at this stage; and second, the iso-surfaces of $\tau = 0$ are approximately parallel to the sloping bottom. In fact, all of the iso-surfaces of positive temperatures within the thermal boundary layer are parallel to the sloping bottom at the early stage, suggesting that the entire thermal boundary layer is parallel to the bottom, and thus the variation of the heat flux boundary condition along the sloping bottom is insignificant. A similar result has been observed in the experiment [7], which showed that the thickness of the thermal boundary layer was growing on a scale of $O((kt^*)^{1/2})$, and the variation of the thickness along the boundary layer was minimal. It is also found in the present simulation that the iso-surfaces of temperatures outside the thermal boundary layer are horizontal (not shown in Fig. 2a), indicating a very weak stratification caused by direct absorption of the radiation by the water body.

The growth of the thermal boundary layer along the slope can also be observed in Fig. 2c and d, which plot a series of temperature profiles along the vertical and horizontal directions. It is seen that large temperature gradients are established in the region near the bottom, while the temperature in other regions is nearly uniform at this early stage (the scales chosen to emphasize the boundary layer are not suitable to demonstrate the previously mentioned weak stratification). The existence of a vertically adverse temperature gradient near the bottom boundary is also clearly demonstrated in Fig. 2c. A similar temperature structure has been revealed in [5] based on an asymptotic solution of the governing equations. The vertically adverse temperature gradient is the direct cause of the convective instability discussed below, while the horizontal temperature gradient is the initial driving force of a large-scale circulation in the enclosure.

3.1.2. Inception of the circulation

As noted previously, a distinct horizontal temperature gradient develops within the thermal boundary layer at the early stage. This temperature gradient then initiates a flow up the slope. In the region near the tip, the boundary layer flow discharges into the core region, and thus an upper intrusion flow travelling from the shallow end to the deep end is formed. As a consequence, a clockwise circulation is established in the enclosure. This is clearly demonstrated in Fig. 3a and b, which presents the velocity field and streamlines in a sectional plane at halfway along the transverse direction. Since the flow is 2-D at this stage, there is no flow in the transverse direction, and thus all the velocity vectors stay within the sectional plane. A flow structure comprising only a single 2-D circulating cell can be identified from Fig. 3a and b.

It is also seen from the velocity field in Fig. 3a that the flow in the majority of the domain is very weak at $t = 0.001$. Distinct flow motions are seen in the bottom boundary layer and near the shallow end. Due to the fluid being drawn by the up-sloping boundary layer flow, a distinct downward flow is also seen at the deep end. As time moves on, more and more fluid in the core region is accelerated (see Fig. 3b). Fig. 3a and b also demonstrate that the center of the circulating cell gradually moves away from the sloping bottom. This is due to the growth of the thermal boundary layer, and also indicates that the large-scale circulation is primarily induced by the temperature gradient in the boundary region.

Fig. 3c and d plot a series of velocity profiles (u and v only since $w = 0$) along the vertical line $(x, z) = (5.5, 2.5)$ at various times of the early stage. These velocity profiles clearly demonstrate the existence of a secondary viscous layer above the sloping bottom. Within the viscous layer, the flow is travelling up the slope ($u < 0$ and $v > 0$). At $t = 0.001$, a local flow up the slope is clearly seen in a thin layer above the bottom. Apart from this layer, the velocity is essentially uniform over the depth at this time. As time moves on, the viscous layer expands rapidly, and the flow up the slope accelerates, as does the core flow. It is also noteworthy that the maximum value of $|v|$ is approximately an order of magnitude smaller than that of $|u|$. The ratio $|v|/|u|$ is coincidently the same as the bottom slope ($A = 0.1$ in this case). This result confirms that the upwelling flow is approximately parallel to the sloping bottom at the early stage.

The asymptotic solution of Farrow and Patterson [5] also revealed similar features of the velocity field in a triangular domain subject to surface radiation. Since a semi-infinite wedge is considered in [5], the temperature

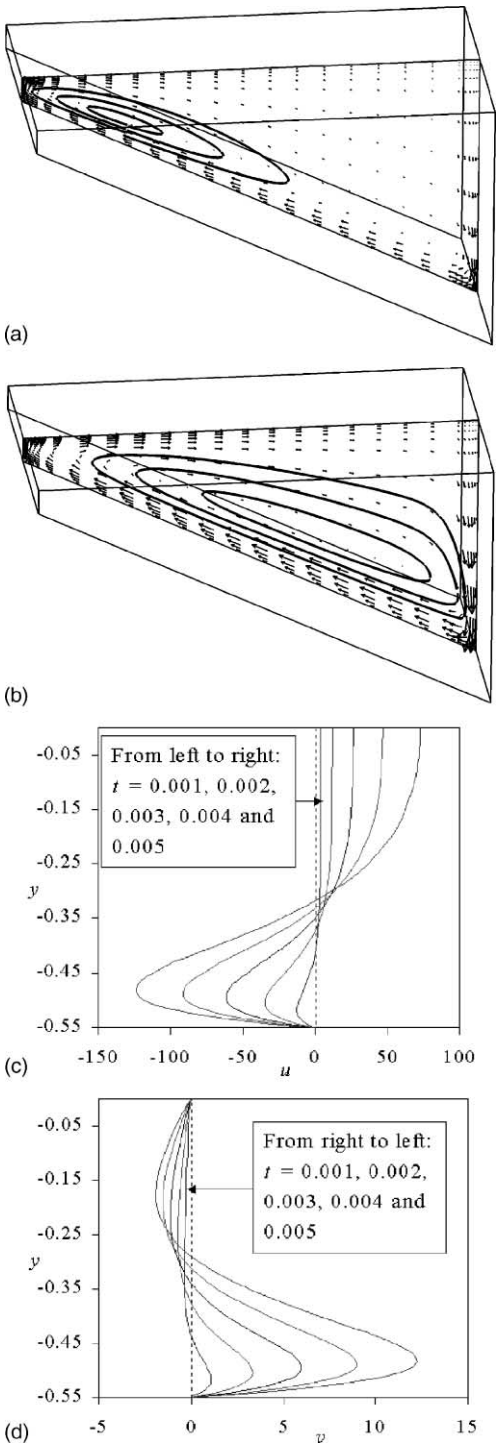

Fig. 3. Velocity field at the early stage. (a) and (b) Velocity vectors and streamlines. (a) $t = 0.001$. (b) $t = 0.003$. (c) and (d) Velocity profiles along the straight line $(x,z) = (5.5, 2.5)$. (c) Horizontal velocity component. (d) Vertical velocity component.

structures can be divided into two distinct regions at any particular time, one with vertical isotherms and the other with horizontal isotherms. In the former region the horizontal temperature gradient drives the circulation, while in the latter region the Phillips mechanism [12,13] drives the flow. These driving mechanisms are justified in terms of the large-time behaviour, but do not apply to the early flow development, especially for the shallow region considered here. As can be seen in Fig. 2, the iso-surfaces of temperatures in the early stage are neither vertical nor horizontal but parallel to the sloping bottom due to the development of the thermal boundary layer. Therefore, the initial driving force of the upwelling circulation must come from the horizontal temperature gradient within the thermal boundary layer.

3.2. Transitional flow

For the present flow parameters, two different types of flow instabilities are observed from the 3-D calculation at the transitional stage, the first a 2-D flow instability and the second a 3-D Bénard type instability.

3.2.1. 2-D flow instability

The 2-D flow instability, which manifests itself in a form of hydraulic-jump like structure, starts from the very deep corner (see Fig. 4a for the temperature structure at $t = 0.006$ or $t^* = 151$ s). This instability is evidently due to the discontinuity of the thermal boundary conditions at this corner. As mentioned in Section 2, an adiabatic wall is assumed at the deep end, whereas a constant heat flux condition applies to the sloping bottom. It has been observed in the previous section that a thermal boundary layer is developing along the sloping bottom, creating iso-surfaces approximately parallel to the bottom. However, the adiabatic boundary condition at the end-wall requires the iso-surfaces there to be normal to the end-wall. Therefore, there is some adjustment of the temperature structure near the deep corner, resulting in an additional thermal boundary layer along the end-wall. These two boundary layers are governed by different mechanisms, and thus they are growing on different scales. The discontinuity of the thickness of the thermal boundary layers at the deeper corner then triggers the 2-D instability under a critical condition while the flow is changing its direction there. As a consequence, the jump like structure is generated.

As time moves on, the jump like structure amplifies and moves downstream (up the slope) along the bottom boundary layer (see the structure at $t = 0.009$ or $t^* = 227$ s in Fig. 4b). Since the above-mentioned perturbation is purely 2-D, the flow remains 2-D at this stage (Fig. 4a and b). A similar structure was also present in the 2-D simulation [8], but it could not be distinguished from the

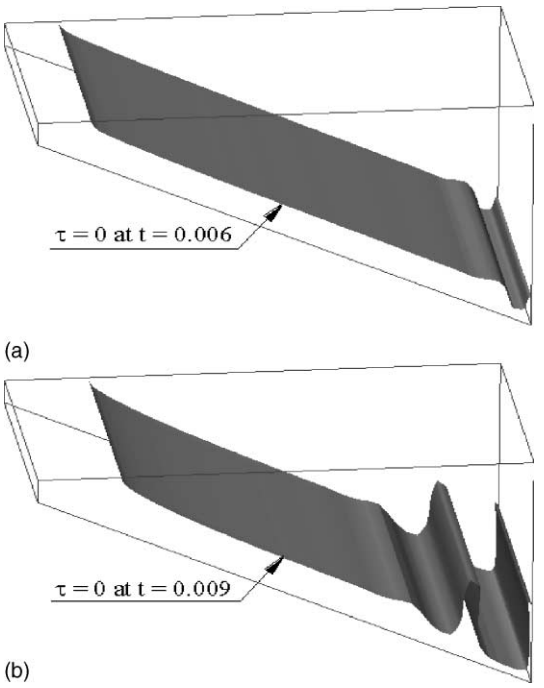

Fig. 4. Flow structures with the presence of a 2-D instability. (a) Temperature iso-surface at $t = 0.006$ ($t^* = 151$ s). (b) Temperature iso-surface at $t = 0.009$ ($t^* = 227$ s).

3-D structures (see below) due to the nature of the 2-D calculation.

3.2.2. 3-D Bénard type instability

While the 2-D jump like structure is being amplified, it increases the local Rayleigh number by increasing the local thickness of the thermal boundary layer. Eventually, this structure becomes unstable to the Rayleigh–Bénard instability. This is demonstrated in Fig. 5a (for $t = 0.0102$ or $t^* = 258$ s), in which a line of warm water has been released from the jump like structure into the upper cold layer. It is interesting to note that the local flow remains 2-D at this time though three-dimensionality is developing in the wedge.

In the meantime, residual radiation continues to be absorbed by the sloping bottom, and heat continues to be diffused into the thermal boundary layer while the surface radiation is maintained. Therefore, the thermal boundary layer keeps growing. As a consequence, the Rayleigh–Bénard instability is also developing across the entire bottom boundary layer. At certain stage, the Rayleigh–Bénard instability will manifest itself as vertical convection. In the shadowgraph visualisation, distinct plumes of warm water, indicated by gradually strengthening dark bands on the shadowgraphs (see Fig. 5c), were seen to arise from the bottom thermal layer after about 60 s after initiation of the surface radiation

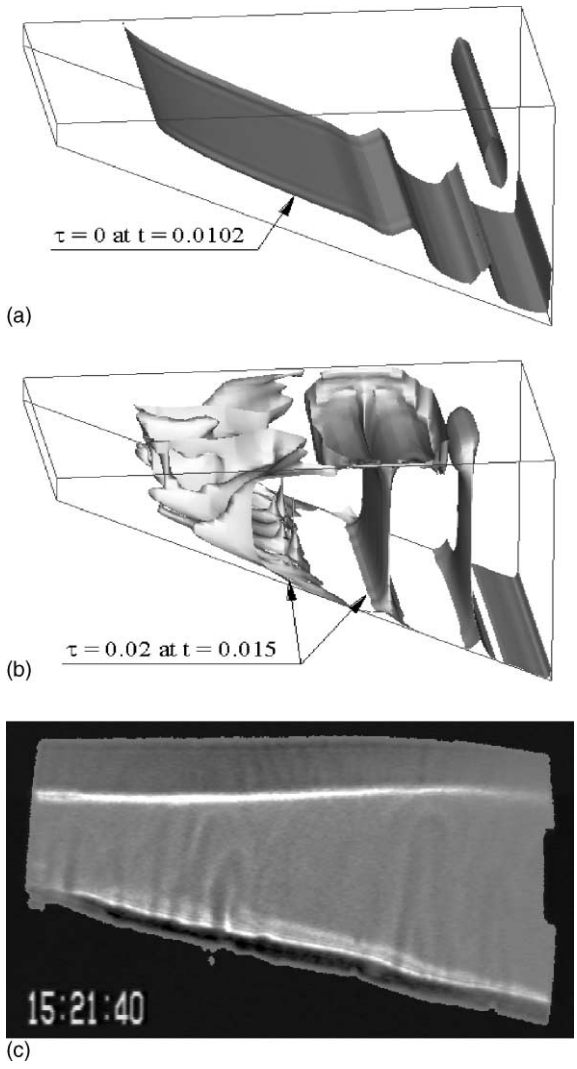

Fig. 5. Flow structures with the presence of the Bénard type instability. (a) Temperature iso-surface at $t = 0.0102$ ($t^* = 258$ s). (b) Temperature iso-surface at $t = 0.015$ ($t^* = 379$ s). (c) Shadowgraph at 100 s.

[7]. The same phenomenon is also observed here in the numerical simulation, although at a later time, as discussed above.

Fig. 5b presents the temperature structure obtained at $t = 0.015$ ($t^* = 379$ s), showing the occurrence of rising plumes. It is seen in this figure that warm water is rising from the bottom thermal layer at different locations in the domain, and the flow has become fully 3-D at this time. In the region near the shallow end, the flow is turning approximately 180°. The combined turning and uprising motions of the flow result in a complicated structure there. In the deeper region, 3-D structures in the form of rising plumes are present. Since the upper

fluid layer is cold at this stage, the plumes are seen to penetrate through the entire local depth of the water column, which is consistent with the shadowgraph observation at the same stage [7]. At this time, the intensive occurrence of rising plumes has destroyed the bottom thermal layer. It is noteworthy that the burst of rising plumes is not regular; there are no fixed locations and frequencies in this process. In addition, it is observed both numerically and experimentally that the rising plumes are carried by the primary circulation up the slope. Therefore, no stable configuration of the temperature structure will be reached. However, a quasi-steady state pattern will be reached at a later stage (see Section 3.3).

The observed convective instability in the form of rising plumes exhibits many features of the intermittent convection observed by Sparrow et al. [14] and later discussed by Foster [15]. However, the difference between the present and the early observations are also distinct. Sparrow et al. observed the plumes occurring from a horizontal fluid layer heated from below, in which there is no primary flow except the convection due to instability, and found that the bursts of plumes have fixed locations once established [14]. In the present case, a primary circulation is established in the wedge prior to the onset of the instability, which drags the rising plumes up the slope in the later stage. Therefore, the bursts of plumes have no fixed locations. Horsch and Stefan [1] have observed similar flow structures in a numerical simulation of littoral waters subject to surface cooling. In that case, the primary circulation is travelling down the slope instead of up the slope, and the plumes are formed in a cooling layer under the water surface and are sinking down into the lower warm layer.

It is worth noting here that the above observations of the transitional flow development is based on the present 3-D numerical simulation, in which a periodic boundary condition is assumed in the transverse direction, and there is no artificial perturbation imposed on either the boundaries or the interior flow. In this case, the only 3-D perturbation that may trigger the 3-D convective instability comes from the accumulation of numerical errors, which is relatively small when compared with the 2-D perturbation discussed above. Therefore, the onset of the Bénard type instability clearly lags behind the 2-D instability. This may not be the case in the experiment or reality. In the experiment described in [7], a water body in a tank with rigid non-slip sidewalls was exposed to the radiation. With this configuration, the non-slip wall boundary condition partly contributed to the 3-D perturbations. There were also many other possible sources of 3-D perturbations in the experiment. With these 3-D perturbations in place, the onset of the 3-D convective instability clearly occurred earlier in the experiment than the time predicted here. Since the 2-D instability was expected only for a short time in the early transitional stage, it may not be distinguishable from the 3-D instability in the experiment. In addition, the shadowgraphs obtained from the experiment represented a transversely integrated temperature structure. This would make it even more difficult to distinguish the 2-D instability from the 3-D plumes.

3.3. Quasi-steady flow

In the transient process, heat is conducted into the ower layer of the water body from the sloping bottom, and consequently a thermal boundary layer is generated and grows along the bottom. In the meantime, a buoyancy-driven flow is initiated within the thermal boundary layer and an upper intrusion flow is formed from the discharge of the boundary layer flow. Therefore, heat is convected away from the boundary layer by the large-scale circulation. In the present case, the convective instability sets in at certain stage due to the build-up of an adverse temperature gradient in the boundary layer, and thus heat is also convected vertically by the secondary motion containing rising plumes and return flows. Both the primary and secondary convective motions result in a significant increase of the temperature in the upper water layer. At some stage, the heat conducted into the thermal boundary layer is balanced by that convected away from it, and thus the growth of the thermal boundary layer ceases. This process has been clearly observed from the shadowgraph visualisation [7]. The horizontal temperature gradient in the boundary layer will maintain a steady up-slope flow, while the vertical adverse temperature gradient may maintain a secondary motion. Therefore, a quasi-steady state is reached.

3.3.1. Flow structure at the quasi-steady state

The typical flow structures at the quasi-steady state are shown in Fig. 6, which presents the calculated isosurfaces of temperatures at $t = 0.2$ and 0.21 ($t^* = 5049$ and 5302 s) as well as two shadowgraph images at the same stage. At this stage, the primary circulation is fully established in the enclosure, which is maintained by distinct horizontal temperature gradients in both the upper water layer and the thermal boundary layer (refer to Fig. 7b). The overall flow structure does not change significantly at the quasi-steady stage (see Fig. 6a and b). However, the detail of the flow structure is modified by the intermittent bursts of rising thermals along the thermal boundary layer. The intermittent convection is governed by a cyclic process as described by Foster [15]: the formation of a thermal boundary layer by diffusion, the instability of this layer when it becomes sufficiently thick, the destruction of the layer by convection, the dying down of the convection and the reformation of the thermal boundary layer by diffusion. The quasi-steady flow shown here also shares the experimentally observed

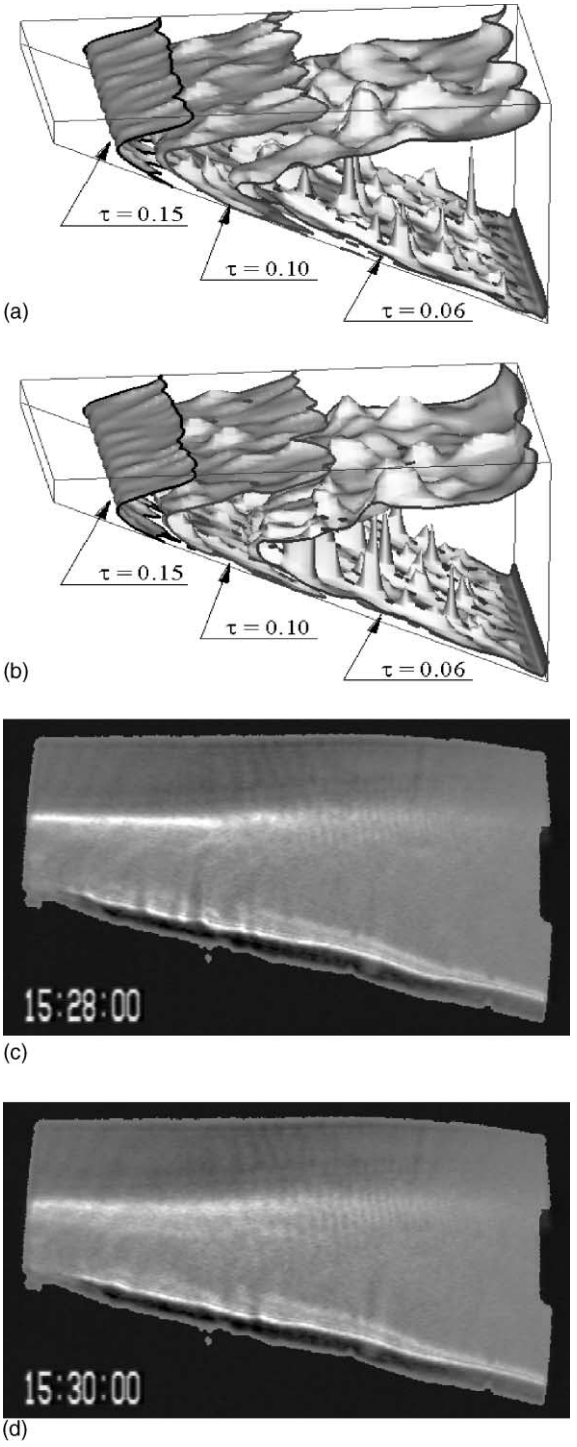

Fig. 6. Typical temperature structures at the quasi-steady state. (a) Temperature iso-surfaces at $t = 0.20$ ($t^* = 5049$ s). (b) Temperature iso-surfaces at $t = 0.21$ ($t^* = 5302$ s). (c) Shadowgraph at 480 s. (d) Shadowgraph at 600 s.

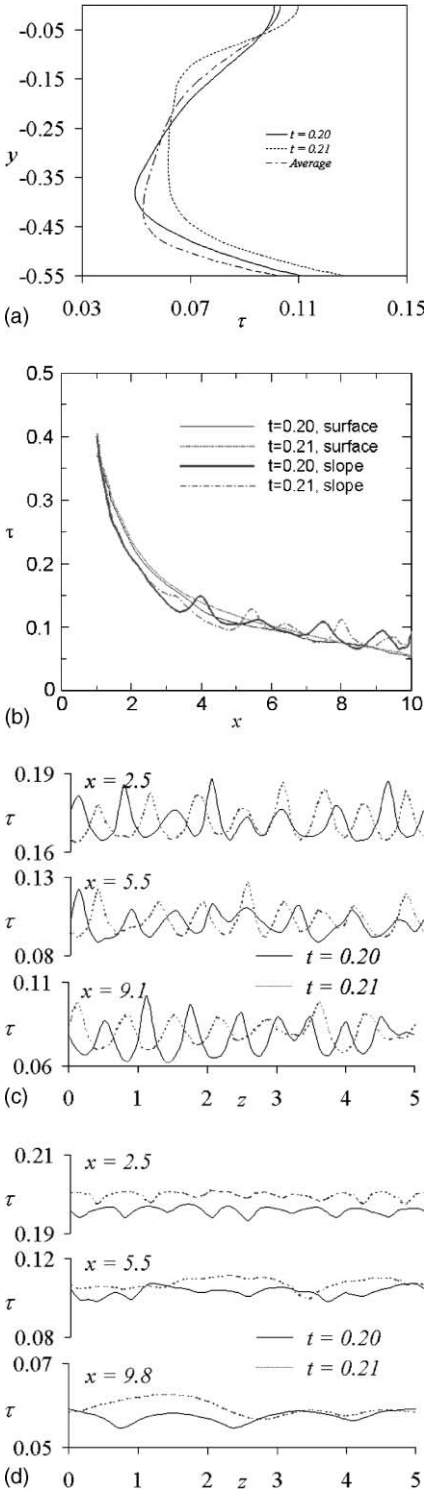

Fig. 7. Temperature profiles extracted at $t = 0.200$ and 0.210. (a) Temperature profiles along the vertical line $(x, z) = (5.5, 2.5)$. (b) Temperature profiles along the water surface and the slope at $z = 2.5$. (c) Temperature profiles along transverse lines on the sloping bottom. (d) Temperature profiles along transverse lines at the water surface ($y = 0$).

features of a bottom-heated convective layer between two horizontal parallel plates [16].

A comparison between Figs. 5 and 6 indicates that the secondary convection, comprising of more or less regularly spanned convection cells, is also well established at the quasi-steady stage. Clearly, the secondary convection in the upper water layer has a dominant wavelength along the transverse direction near both the shallow and deep ends (Fig. 6a and b). In fact, there is also a dominant transverse wavelength for the entire thermal boundary layer (also see Fig. 7c and corresponding discussion). It is also seen in Fig. 6a and b that the transverse wavelength for the upper layer increases along the streamwise direction (also refer to Fig. 7d). The comparison between Figs. 5 and 6 also indicates that the intensity of the secondary convection is reduced at the quasi-steady stage. This is due to the development of a stabilising upper layer underneath the water surface (refer to Fig. 7a), which tends to suppress the secondary convection. At this stage, the rising thermals disperse completely before reaching the water surface, in contrast to the penetration of the entire depth in the transitional stage. This is exactly what has been observed in the shadowgraph visualisation at later stages (see Fig. 6c and d and also [7]).

3.3.2. Temperature profiles

The temperature profiles along the horizontal, vertical and transverse directions at two time instances of the quasi-steady state ($t = 0.20$ and 0.21, corresponding to Fig. 6a and b) are plotted in Fig. 7. Fig. 7a presents the temperature profiles extracted along the vertical line $(x, z) = (5.5, 2.5)$ near the centre of the enclosure. A time-averaged temperature profile (for $t = 0.18$–0.22) is also plotted in Fig. 7a. It is clear in Fig. 7a that the temperature structure near the centre of the enclosure is characterised by three layers: an upper layer with a favourable temperature gradient, a lower layer with an adverse temperature gradient and an intermediate layer between the upper and lower layers. Similar temperature structure was observed in a bottom-heated horizontal fluid layer [16]. A comparison between the temperature profiles at this and early stages (see Figs. 2c and 7a) indicates that the upper water layer has been heated significantly, and thus the temperature in the upper fluid layer is comparable with that in the thermal boundary layer at the quasi-steady stage. The adverse temperature gradient in the lower layer is responsible for the secondary convection, whereas the favourite temperature gradient in the upper layer tends to suppress the secondary convection.

Fig. 7b presents the temperature profiles along the water surface and the slope at $z = 2.5$, which indicate the existence of a distinct horizontal temperature gradient across the enclosure. It is clear that the horizontal temperature gradient is greatest near the tip, and reduces gradually with the distance from the tip. As noted previously, a horizontal temperature gradient builds up only in the thermal boundary layer in the early stage. Apart from the boundary region, the temperature isosurfaces in the wedge are horizontal, suggesting that no horizontal temperature gradient exist in the majority of the enclosure in the early stages. However, the situation has changed dramatically at the quasi-steady state, at which a distinct horizontal temperature gradient is observed in the upper layer (see Fig. 7b) in addition to a horizontal temperature gradient in the thermal boundary layer. These two horizontal temperature gradients maintain respectively a steady up-slope flow along the bottom and a steady outflow from the tip region, which in turn form the large-scale primary circulation in the wedge at the quasi-steady state. Fig. 7b also indicates that the surface temperature only slightly changes with time at this stage (note that the temperature here is obtained by solving the quasi-steady temperature equation (13) in which the linear growth of the spatially averaged temperature is excluded).

The features of the secondary convection in the transverse direction, particularly the transverse wavelength can be observed in Fig. 7c and d, which plot the temperature profiles along the transverse direction at different locations. Fig. 7c plots the temperature profiles at three locations on the sloping bottom, while Fig. 7d plots the temperature profiles at three locations at the water surface. The horizontal locations are selected so that the flow features near both the shallow and deep ends as well as the centre of the domain are demonstrated. It is observed in Fig. 7c that all the temperature profiles comprises of equal number of peaks, suggesting that the secondary convection within the bottom thermal boundary layer has a dominant wavelength along the transverse direction, and this wavelength does not change with time at the quasi-steady state. Within the upper water layer, the secondary convection also has a dominant transverse wavelength near the shallow end (e.g. $x = 2.5$ in Fig. 7d), which is the same as that of the thermal boundary layer. However, the transverse wavelength increases along the streamwise direction within the upper water layer (see Fig. 7d), which is possibly due to the merger of convection cells as the water depth increases. At locations near the centre of the enclosure (e.g. $x = 5.5$), the ongoing merger causes irregular appearance of the temperature profiles, whereas at locations near the deep end (e.g. $x = 9.8$), the temperature profiles becomes regular again, and clearly there is a dominant transverse wavelength at this location. The transverse wavelength of the secondary convection near the deep end is more than double the wavelength near the shallow end. A stability analysis specifically focusing on the features of the secondary convection will be reported separately.

3.4. Comparisons with a 2-D simulation

In this section, the present 3-D simulation is compared with the previously reported 2-D simulation [8].

3.4.1. Flow development and structures at different stages

For an initially isothermal and stationary water body in a wedge, three distinct stages of the flow development due to the absorption of radiation have been observed based on the present 3-D simulation, i.e. an initial growth stage, a transitional stage and a quasi-steady stage. The initial stage is dominated by conduction at the bottom boundary, resulting in a thermal boundary layer growing there, and the flow is purely 2-D. The transitional stage is characterised by the presence of flow instabilities, first a 2-D instability, and then a 3-D Bénard type instability which is manifested as rising plumes emanating from the boundary layer and translating up the slope. The quasi-steady state is characterised by a steady rise in the average temperature, a circulation that encompasses the full region and quasi-regular presence of the convective instability with a reduced intensity. At this stage, the flow is fully 3-D across the domain.

The present observation of the three-stage development of the convective circulation agrees favourably with the previous 2-D simulation [8]. At the early stage when the flow is 2-D, the 2-D simulation gives the same prediction as the 3-D calculation. Although the convective flow becomes 3-D as a consequence of the onset of instability, the nature of the convective instability in the form of rising plumes allows the 2-D simulation to capture certain important features of the instability. Both the 2-D and 3-D simulations agree qualitatively well with the shadowgraph flow visualisation [7].

3.4.2. Time history of temperatures within the thermal boundary layer

Fig. 8a and b compare the 3-D prediction of temperatures within the thermal boundary layer (~2 mm above the sloping bottom) with the data obtained from the previous 2-D simulation [8] and experimental measurements [7]. Here, the experimental data is normalised with the scales described in Section 2, and the numerical data is recovered from the quasi-steady state solution. Excellent agreement between the 2-D and 3-D simulations can be seen throughout the calculation. The numerical data also agrees well with the experimental measurements in a qualitative sense despite certain discrepancies between the simulation and experiment. Both numerical and experimental results reveal a three-stage development of the flow, and they both indicate that the frequency of the secondary convection increases toward the shallow end. The discrepancies between the numerical simulations and the experiments may be attributed to many factors, including heat conduction across the

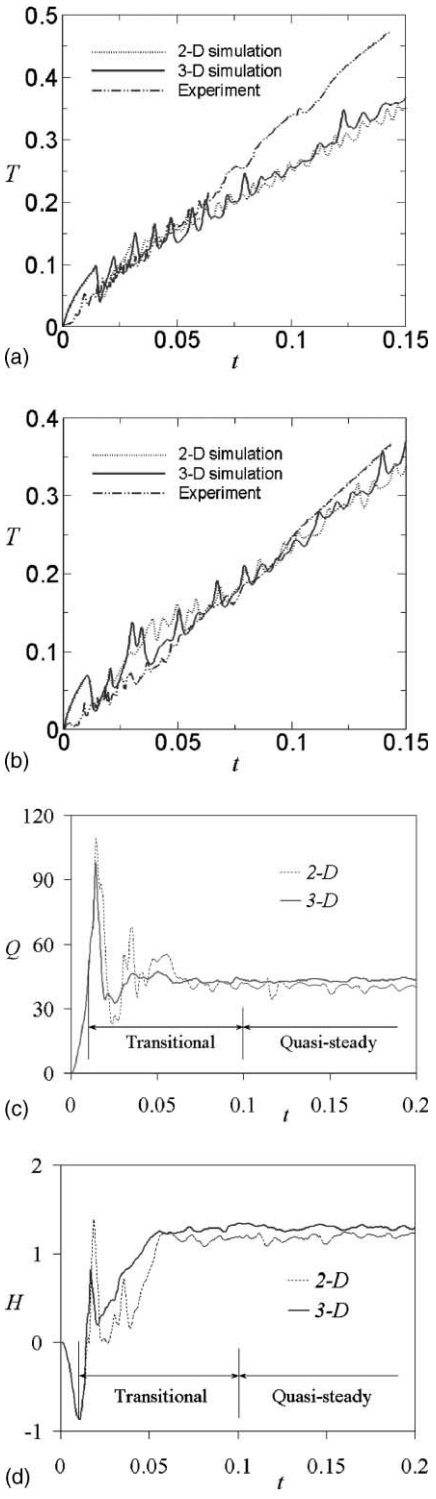

Fig. 8. Time series of (a) temperature in the thermal boundary layer at $x = 4.25$; (b) temperature in the thermal boundary layer at $x = 6.75$; (c) integrated horizontal flow rate and (d) integrated horizontal heat transfer rate.

walls and surface of the experimental configuration, errors in the determination of flow and fluid properties, and determination of the input radiation in the experiment. Further experimental and numerical investigations are required to clarify these discrepancies. The important point here is that both experiment and simulation show the same broad features of flow development.

3.4.3. Volumetric flow rate and horizontal heat transfer

The volumetric flow rate (or the strength of the circulation) and horizontal heat transfer rate are the two quantities of practical interests. They are defined in a 2-D domain as [2]

$$Q(x) = \frac{1}{2}\int_{-Ax}^{0} |u|\,\mathrm{d}y, \qquad H(x) = \int_{-Ax}^{0}\left(uT - \frac{\partial T}{\partial x}\right)\mathrm{d}y \tag{15}$$

where $Q(x)$ and $H(x)$ are respectively the volumetric flow rate and heat transfer rate across a vertical sectional plane at a given x location. In a 3-D domain, these quantities are defined as

$$Q(x) = \frac{1}{2W}\int_{0}^{W}\int_{-Ax}^{0} |u|\,\mathrm{d}y\,\mathrm{d}z, \qquad H(x) = \frac{1}{W}\int_{0}^{W}\int_{-Ax}^{0}\left(uT - \frac{\partial T}{\partial x}\right)\mathrm{d}y\,\mathrm{d}z \tag{16}$$

In Eqs. (15) and (16), the dimensionless quantities Q and H represent the corresponding dimensional quantities normalised by the scales k and $I_0 h^*$ respectively. An averaged volumetric flow rate Q and an averaged heat transfer rate H can be obtained by integrating these quantities along the horizontal direction as follows:

$$Q = \frac{1}{L}\int_{0}^{L} Q(x)\,\mathrm{d}x, \quad H = \frac{1}{L}\int_{0}^{L} H(x)\,\mathrm{d}x \tag{17}$$

The time histories of the averaged flow rate and heat transfer rate obtained from both 2-D and 3-D simulations are plotted in Fig. 8c and d. All these plots confirm the three stages of the flow development (the transitional and quasi-steady stages are approximately indicated in the plots). It is seen in Fig. 8c that the average volumetric flow rate increases gradually at early stage until it reaches a very high peak value. Then, there is a sudden drop in the flow rate and a subsequent fluctuation. In the transitional stage, the fluctuation of the flow rate is strong and irregular. After a quasi-steady state is reached, the average flow rate oscillates about a stable mean value with reduced amplitude. Similar features can be observed for the averaged heat transfer rate (Fig. 8d). At early times, an imbalance between a strong up-slope flow of hot water ($uT < 0$) in the boundary layer and a weak return flow of cool water in the bulk of the domain results in a negative heat transfer rate ($H < 0$). The switch from the initial growth stage to the transitional stage corresponds approximately to the presence of the first dip in the plots of the heat transfer rate, since which the mean heat transfer rate climbs and eventually becomes positive. Both 2-D and 3-D calculations predict that the switch from the initial stage to the transitional stage occurs at approximately $t = 0.011$ ($t^* = 278$ s). The time series plotted in Fig. 8 suggests that a quasi-steady state is reached at a time after $t = 0.10$ (about 42 min in real time).

It is seen in Fig. 8 that the flow and heat transfer rates predicted in the 3-D simulation are slightly higher than those predicted in the 2-D simulation. The difference in the time-averaged values (from $t = 0.18$ to 0.22) is about 10% for the flow rate and 6% for the heat transfer rate. It is also noteworthy in Fig. 8 that the calculated flow and heat transfer rates from the 3-D simulation fluctuate at smaller amplitudes than those calculated from the 2-D simulation at both transitional and quasi-steady stages. This is because the quantities from the 3-D simulation are averaged over the transverse direction, whereas those from the 2-D simulation are representative of the values on a single sectional plane.

3.5. Dependence on grid resolution and time step

The previous numerical results are obtained from an $81 \times 61 \times 41$ mesh with 81 nodes over the length (L), 61 nodes over the depth (h) and 41 nodes over the width (W). This mesh is selected based on the results of a mesh and time-step dependence test, for which three meshes are tested with different time steps (see Table 1). For the coarsest mesh (Mesh 1), both the grid spacing and the calculation time step are doubled from those for the finest mesh (Mesh 3). Therefore, the CFL (Courant–Freidrich–Levy) number remains the same for the calculations with Mesh 1 and Mesh 3.

The calculated horizontal flow and heat transfer rates with different meshes are plotted in Fig. 9a and b, and the time-averaged values at the quasi-steady state are listed in Table 1. It can be seen in Fig. 9 that the solutions with all meshes indicate three stages of the flow development as noted previously. In the initial growth

Table 1
Parameters and results of mesh and time-step dependence test

	Mesh	Time step ($\times 10^{-6}$)	Time-averaged results at the quasi-steady state	
			Q	H
1	$41 \times 31 \times 21$	2.0	42.19	1.272
2	$61 \times 46 \times 31$	1.5	43.55	1.327
3	$81 \times 61 \times 41$	1.0	43.46	1.293
Maximum variations (%)			3.1	4.3

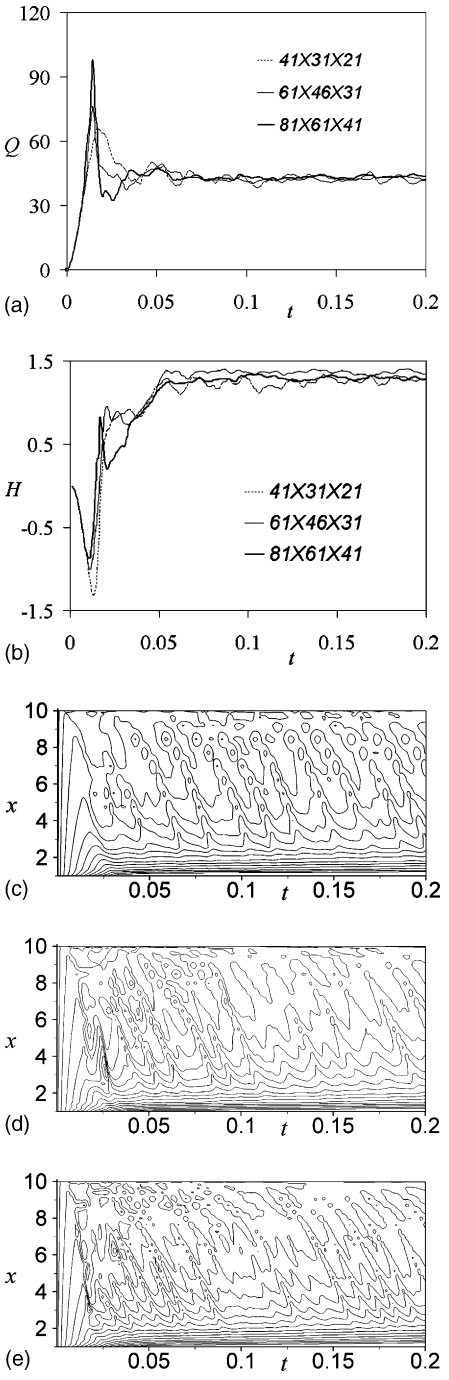

Fig. 9. (a) Time series of integrated horizontal flow rate. (b) Time series of integrated horizontal heat transfer rate. (c)–(e) Time evolution of temperatures on the sloping bottom at $z = 2.5$. The contour interval is 0.02. (c) Results by $41 \times 31 \times 21$ mesh. (d) Results by $61 \times 46 \times 31$ mesh. (e) Results by $81 \times 61 \times 41$ mesh.

stage, the solutions follow closely to each other. There is a slight discrepancy among the solutions in the predicted starting time of the transition, and somewhat larger discrepancies are found in the transitional stage. In the quasi-steady state, all solutions show a similar flow pattern with intermittent bursts of rising thermals, and the predicted time-averaged quantities are reasonably close (see Table 1).

Fig. 9c–e demonstrate the variations of local flow structures. Plotted here are the time evolutions of the calculated temperatures on the sloping bottom at $z = 2.5$, showing spatial and temporal variations as well as fluctuations associated with the convective instability. It is clear that the same flow pattern is revealed by all meshes. It is also noticeable that the spatial and temporal scales (wavelength and period) related to the instability depend on the grid resolution. There are large discrepancies between the finest mesh and the coarsest mesh. However, the discrepancies between the two finer meshes are evidently smaller. To precisely resolve the wavelength and other properties of the instability, which is beyond the scope of the present investigation, higher grid resolution may be required. Since the purpose of the present study is to identify the major features of the flow development rather than resolve every detail of the convective instability, the $81 \times 61 \times 41$ mesh is sufficient for this purpose.

4. Conclusions

The present paper considers the natural convection in a shallow wedge subject to solar radiation. The primary purpose of this study is to demonstrate by means of direct numerical simulations the important features of the flow development. A similar problem has been considered by Farrow and Patterson [5]. However, Farrow and Patterson considered a semi-infinite wedge which comprises of both shallow and deep waters in terms of the relative scales of the maximum water depth and the penetration depth of the radiation [5], whereas the present study focuses on very shallow waters and considers an fully enclosed domain. A corresponding flow visualisation [7] and a 2-D numerical simulation [8] have been reported previously.

The results of the present 3-D calculation reveal that the development of the convective circulation in the water body from an isothermal and stationary state passes through three distinct stages: an initial stage, a transitional stage and a quasi-steady stage. The initial stage is characterised by domination by conduction at the bottom boundary, which then forms a thermal boundary layer along the sloping bottom. A primary circulation is initiated by the temperature gradient in the thermal boundary layer. The transitional stage is characterised by the presence of instabilities, first a 2-D instability, and then a 3-D Bénard type instability which

manifests as rising plumes emanating from the bottom boundary and translating up the slope. The quasi-steady state is characterised by a steady rise in average temperature, a circulation which encompasses the full region and quasi-regular presence of instabilities with reduced intensities.

The above findings have confirmed the earlier observations in a physical experiment [7]. In addition, a comparison between the 3-D and 2-D calculations has revealed that the 2-D simulation is able to capture the major features of the flow development, including the basic features of the flow instabilities, and thus can be used to extract additional flow details with confidence. However, the nature of the 2-D model would not allow a full resolution of the details of the 3-D convective instability.

It must be recognised that only one single parameter set is reported here, chosen so that the main features occur. A number of other parameter regimes may occur which show different subsets of the present behaviour. A scaling and numerical analysis that identifies these regimes and their characteristic behaviour can be found in [6].

Acknowledgements

This research was financially supported by the Australian Research Council (ARC) through an Australian Postdoctoral Fellowship scheme. The numerical simulations were carried out on the High Performance Computing facilities jointly funded by the ARC and James Cook University. The authors are also grateful to the valuable comments from the anonymous reviewers.

References

[1] G.M. Horsch, H.G. Stefan, Convective circulation in littoral water due to surface cooling, Limnology and Oceanography 33 (5) (1988) 1068–1083.

[2] G.M. Horsch, H.G. Stefan, S. Gavali, Numerical simulation of cooling-induced convective currents on a littoral slope, International Journal for Numerical Methods in Fluids 19 (1994) 105–134.

[3] D.E. Farrow, J.C. Patterson, On the response of a reservoir sidearm to diurnal heating and cooling, Journal of Fluid Mechanics 246 (1993) 143–161.

[4] D.E. Farrow, J.C. Patterson, On the stability of the near shore waters of a lake when subject to solar heating, International Journal of Heat and Mass Transfer 36 (1) (1993) 89–100.

[5] D.E. Farrow, J.C. Patterson, The daytime circulation and temperature structure in a reservoir sidearm, International Journal of Heat and Mass Transfer 37 (13) (1994) 1957–1968.

[6] C. Lei, J.C. Patterson, Unsteady natural convection in a triangular enclosure induced by absorption of radiation, Journal of Fluid Mechanics 460 (2002) 181–209.

[7] C. Lei, J.C. Patterson, Natural convection in a reservoir sidearm subject to solar radiation: experimental observations, Experiments in Fluids 32 (5) (2002) 590–599.

[8] C. Lei, J.C. Patterson, Natural convection in a reservoir sidearm subject to solar radiation: a two-dimensional simulation, Numerical Heat Transfer, Part A. Applications 42 (2002) 13–32.

[9] A. Rabl, C.E. Nielsen, Solar ponds for space heating, Solar Energy 17 (1975) 1–12.

[10] J.T.O. Kirk, Optical limnology – a manifesto, in: P. De Deckker, W.D. Williams (Eds.), Limnology in Australia, CSIRO Australia and Dr. W. Junk Publishers, Melbourne, 1986, pp. 33–62.

[11] C. Lei, L. Cheng, K. Kavanagh, Spanwise length effects on three-dimensional modelling of flow over a circular cylinder, Computer Methods in Applied Mechanics and Engineering 190 (22-23) (2001) 2909–2923.

[12] C. Wunsch, On oceanic boundary mixing, Deep-Sea Research 17 (1970) 293–301.

[13] O.M. Phillips, On flows induced by diffusion in a stably stratified fluid, Deep-Sea Research 17 (1970) 435–443.

[14] E.M. Sparrow, R.B. Husar, R.J. Goldstein, Observations and other characteristics of thermals, Journal of Fluid Mechanics 41 (1970) 793–800.

[15] T.D. Foster, Intermittent convection, Geophysical Fluid Dynamics 2 (1971) 201–217.

[16] O. Manca, B. Morrone, S. Nardini, Experimental analysis of thermal instability in natural convection between horizontal parallel plates uniformly heated, Transactions of the ASME, Journal of Heat Transfer 122 (2000) 50–57.